Korean J. Chem. Eng., 39(6), 1641-1650 (2022)
DOI: 10.1007/s11814-021-1050-7

pISSN: 0256-1115
eISSN: 1975-7220

ZnS-modified carbon nitride nanosheet with enhanced performance of elemental Hg removal: An experimental and density functional theory study

Yang Ling*, Jiang Wu*,*,†, Lingtao Yang***, and Dongjing Liu**,†**

*School of Energy and Power Engineering, University of Shanghai for Science and Technology, Shanghai 200093, China
**School of Energy and Power Engineering, Jiangsu University, Zhenjiang 212013, China
***College of Energy and Mechanical Engineering, Shanghai University of Electric Power, Shanghai 200090, China
(*Received 15 September 2021 • Revised 15 December 2021 • Accepted 22 December 2021*)

Abstract−The emission of mercury from anthropogenic activities is a serious concern in both developed and developing countries due to its high toxicity and persistence. Here, carbon nitride nanosheets (CNNS) were attained via a two-step thermal etching method and applied for Hg^0 removal. Proper deposition of ZnS can markedly reinforce the Hg^0 capture ability of CNNS. 10ZnS/CNNS notably outperforms ZnS and CNNS at 100 °C, which is primarily attributed to surface chemisorbed oxygen species and polysulfide active sites. Besides, Hg^0 adsorption and thermal catalytic oxidation pathways are further disclosed using quantum chemistry calculations based on density functional theory (DFT). The calculation results show that the presence of zinc species is beneficial to the decomposition of adsorbed oxygen, which plays a key role in the catalytic oxidation of Hg^0, thereby contributing to the enhancement of mercury removal performance.

Keywords: Mercury, Metal Sulfide, Density Functional Theory, Chemisorbed Oxygen

INTRODUCTION

Mercury (Hg), as a global pollutant, has attracted increasing attention in the air toxics [1]. Because of its adverse effects on human health and the environment, the abatement of mercury has gained enormous public concern in recent decades [2]. Coal-fired units are the major sources of mercury emission from anthropogenic activity [3]. Three forms of mercury species co-exist in coal-fired flue gas: particulate-bound (Hg^p), oxidized mercury (Hg^{2+}), and elemental mercury (Hg^0) [4]. Hg^p and Hg^{2+} can be easily eliminated by particulate matter (PM) control devices and wet flue gas desulfurization (WFGD) system, respectively. Nevertheless, Hg^0 vapor with high volatility and low water-solubility cannot be captured by conventional air pollution control equipment [5]. Thus, Hg^0 is the dominant mercury species emitted into the atmosphere.

Currently, adsorption and catalytic oxidation methods are two primary mechanisms for Hg^0 emission control. Adsorption technology can concurrently remove Hg^p, Hg^{2+} and Hg^0 species from flue gas by using porous adsorbents [6,7]. Catalytic oxidation is to oxidize insoluble Hg^0 into Hg^{2+}, which is subsequently absorbed in WFGD units [8,9]. In terms of adsorption technology, breakthrough of adsorbents is inevitable when surface active sites are fully occupied by Hg^0 vapor, which hinders its practical application for continuous mercury removal in power plants. In this respect, employment of catalysts can avoid the shortcomings of adsorption technology. Recently, graphitic carbon nitride (g-C_3N_4), as a structural analog of graphene, has been reported to be effective in mercury removal due to its peculiar electronic property and good thermal stability [10-12]. As compared to commonly used activated carbon, g-C_3N_4 has an easier tunable electronic structure, inexpensive synthesis process, and much higher intrinsic Hg^0 affinity [13,14]. Nevertheless, the mercury removal performance of pristine and metal oxide-modified g-C_3N_4 would distinctly deteriorate at elevated temperature and in presence of acidic flue gas constituents [15,16]. Though loading metal sulfides on adsorbent surface can immobilize flue gas mercury and improve its resistance to sulfur dioxide, the Hg^0 removal efficiency would visibly decline when reaction temperature is above 150 °C due to unstable adsorbed mercury species and possible decomposition of metal sulfides [17]. Considering the temperature fluctuation and existence of acidic gas components in coal-fired flue gas, it is imperative to develop catalysts that can stably remove mercury in wider temperature range and complex gas atmosphere. As reported, zinc sulfide (ZnS) is highly active in elevated-temperature range (150-200 °C) but performs poorly at temperatures lower than 150 °C [18]. In this regard, combining ZnS with g-C_3N_4 as a composite catalyst may overcome their drawbacks and make full use of their merits. In addition, dispersing ZnS on the surface of g-C_3N_4 can also achieve a balance between mercury removal performance and cost economy for practical applications [19].

In this work, ZnS/g-C_3N_4 composites were constructed using precipitation approach and employed for capturing Hg^0 vapor. The physiochemical properties were characterized using X-ray diffractometer (XRD), field emission scanning electron microscopy (FESEM), transmission electron microscopy (TEM), and X-ray photoelectron spectroscopy (XPS) techniques. Furthermore, the behavior of Hg^0 adsorption and catalytic oxidation over modified surface was investigated by theoretical calculations based on density functional the-

†To whom correspondence should be addressed.
E-mail: wjcfd2002@163.com, liudongjing19@163.com

ory (DFT). Combining the experimental and theoretical results, the enhancement effect of ZnS on the mercury removal performance of g-C_3N_4 was revealed therewith.

METHODS

1. Preparation and Characterization

Carbon nitride nanosheets (CNNS) were obtained via a two-step thermal etching route, which is described in detail elsewhere [20, 21]. ZnS/g-C_3N_4 composites were prepared using precipitation approach [22]. First, specific quantities of zinc acetate dihydrate ($Zn(CH_3COO)_2{\cdot}2H_2O$, Aladdin, AR) and sodium sulfide nonahydrate ($Na_2S{\cdot}9H_2O$, Aladdin, AR) were put into two beakers, respectively. The one containing $Zn(CH_3COO)_2{\cdot}2H_2O$ was named as beaker A, another containing $Na_2S{\cdot}9H_2O$ was tabbed as beaker B. Then, about 50 g deionized water was poured into the two beakers to yield transparent solutions. As-prepared CNNS was added into beaker A under vigorous stirring for ca. 30 min. After that, the solution in beaker B was added dropwise into beaker A under consecutive stirring. After standing for 2 h, the resulting turbid suspensions in beaker A were filtered, washed with deionized water for three times, and eventually dried at 65 °C for 12 h. The final products were designated as *x*ZnS/CNNS, wherein *x* represented the mass percentage of ZnS in composites. Pure ZnS was also prepared for comparison using similar method. The samples were characterized using XRD, FESEM, TEM, XPS, etc., which is fully described elsewhere [23].

2. Gaseous Elemental Mercury Removal

The Hg^0 removal performance was tested in a bench-scale packed-bed reactor. The schematic and detailed description of elemental mercury removal system is illustrated in Fig. S1 (Supplementary Materials).

3. DFT Calculation Details

The DFT calculation was carried out by using CASTEP (Cambridge Serial Total Energy Package) module. The generalized gradient approximation (GGA) theory was applied with Perdew-Burke-Ernzerhof (PBE) functional method. The convergence criteria for geometric optimization and single point energy calculation were set as follows: maximal energy change of 2.0×10^{-5} eV/atom, maximal force on the atoms of 0.05 eV/Å, maximal stress on the atoms of 0.1 GPa, and maximal atomic displacement of 0.002 Å. The g-C_3N_4 surface with the size of 2×2 was used to simulate the reaction surface [24]. A vacuum layer of 15 Å was used to reduce the interference from adjacent layers. The absorption energy was calculated by:

$$E_{adsorption}=E_{system}-(E_{adsorbate}+E_{carrier}) \quad (1)$$

where $E_{adsorption}$ represents the absorption energy (eV). E_{system} is the total energy (eV) of the system that given molecules adsorbed by carrier surface. $E_{adsorbate}$ and $E_{carrier}$ represent the total energy (eV) of isolated adsorbate and carrier, respectively. The transition state search (TSS) was used to characterize the energy barrier and net heat absorption of reaction processes via linear synchronous transit/quadratic synchronous transit (LST/QST) method. The energy barrier and reaction heat are defined as:

$$E_{barrier}=E_{TS}-E_{reactant} \quad (2)$$

$$E_{reaction}=E_{product}-E_{reactant} \quad (3)$$

where $E_{barrier}$ represents the reaction energy barrier (eV). $E_{reaction}$ is the net heat absorption of a given reaction. E_{TS}, $E_{reactant}$ and $E_{product}$ represent the total energy (eV) of transition states, reactants and products, respectively.

RESULTS AND DISCUSSION

1. Characterization Analysis

The XRD profile in Fig. 1(a) confirms the successful synthesis of g-C_3N_4. The peaks centered at around 12.9 and 27.7° are ascribed to the reflections of the (001) and (002) planes of g-C_3N_4 (JCPDS 87-1526), respectively. The minor peaks at 12.9° are attributed to the planar ordering of tri-*s*-triazine units, while the intense peaks at 27.7° represent the interlayer stacking of g-C_3N_4 aromatic layers. The intense peaks at 28.7, 47.6, 56.4, 77.2° in ZnS relate to the reflections of the (111), (220), (311), (331) panes of sphalerite (JCPDS 01-0792), respectively. After loading onto CNNS, the feature signals of ZnS become weaker, suggesting that ZnS is exists as amorphous phases or highly dispersed on CNNS surface [25]. What is

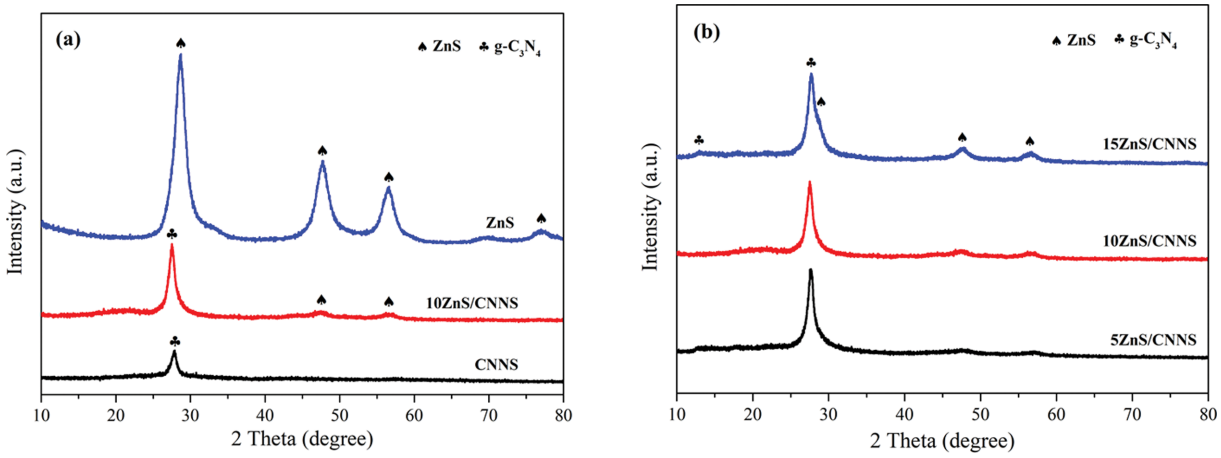

Fig. 1. XRD profiles: (a) ZnS, CNNS and 10ZnS/CNNS; (b) *x*ZnS/CNNS.

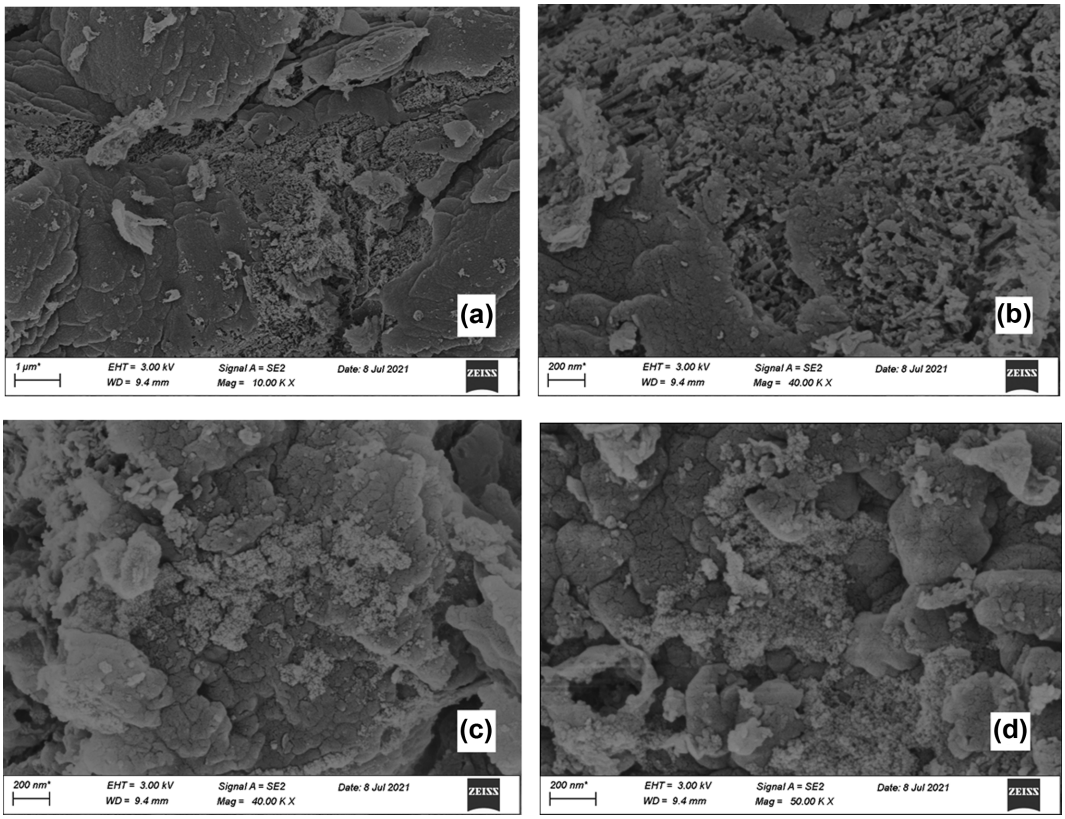

Fig. 2. SEM images: (a), (b) CNNS (c), (d) 10ZnS/CNNS.

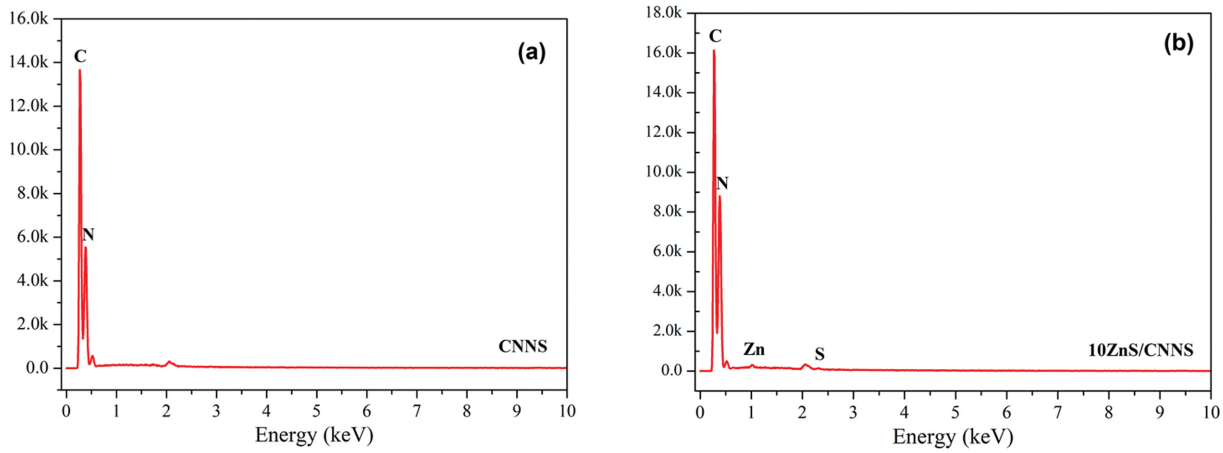

Fig. 3. EDS profiles: (a) CNNS and (b) 10ZnS/CNNS.

more, the characteristic peak intensity of ZnS gradually increases with incremental ZnS loading values (Fig. 1(b)). With respect to pristine CNNS, the diffraction angles of the (002) peaks slightly move toward higher values after modifying with ZnS, indicating a decreased gallery distance between the basic sheets of g-C_3N_4 in *x*ZnS/CNNS [26].

The surface microstructures of CNNS and 10ZnS/CNNS were studied via FESEM technique. As presented in Fig. 2(a), big bulk-like stacks consisting of packed layers with sizes of several microns are observed. Numerous pore structures are also detected on CNNS surface as shown in Fig. 2(b). After loading with 10 wt% ZnS (Fig. 2(c) and (d)), the bulk structure of CNNS remains and the surface becomes more compact. In addition, many tiny aggregates are found on the surface of CNNS, which are possibly assigned to ZnS particles. The energy disperse spectroscopy (EDS) profiles of CNNS and 10ZnS/CNNS are displayed in Fig. 3. Two strong peaks at 0.27 and 0.39 keV are detected in CNNS and 10ZnS/CNNS, which are assigned to the C and N elements of carbon nitrides, respectively. The weak signals of Zn at 1.02 eV and S at 2.31 eV are detected in 10ZnS/CNNS, testifying the successful loading of ZnS on CNNS

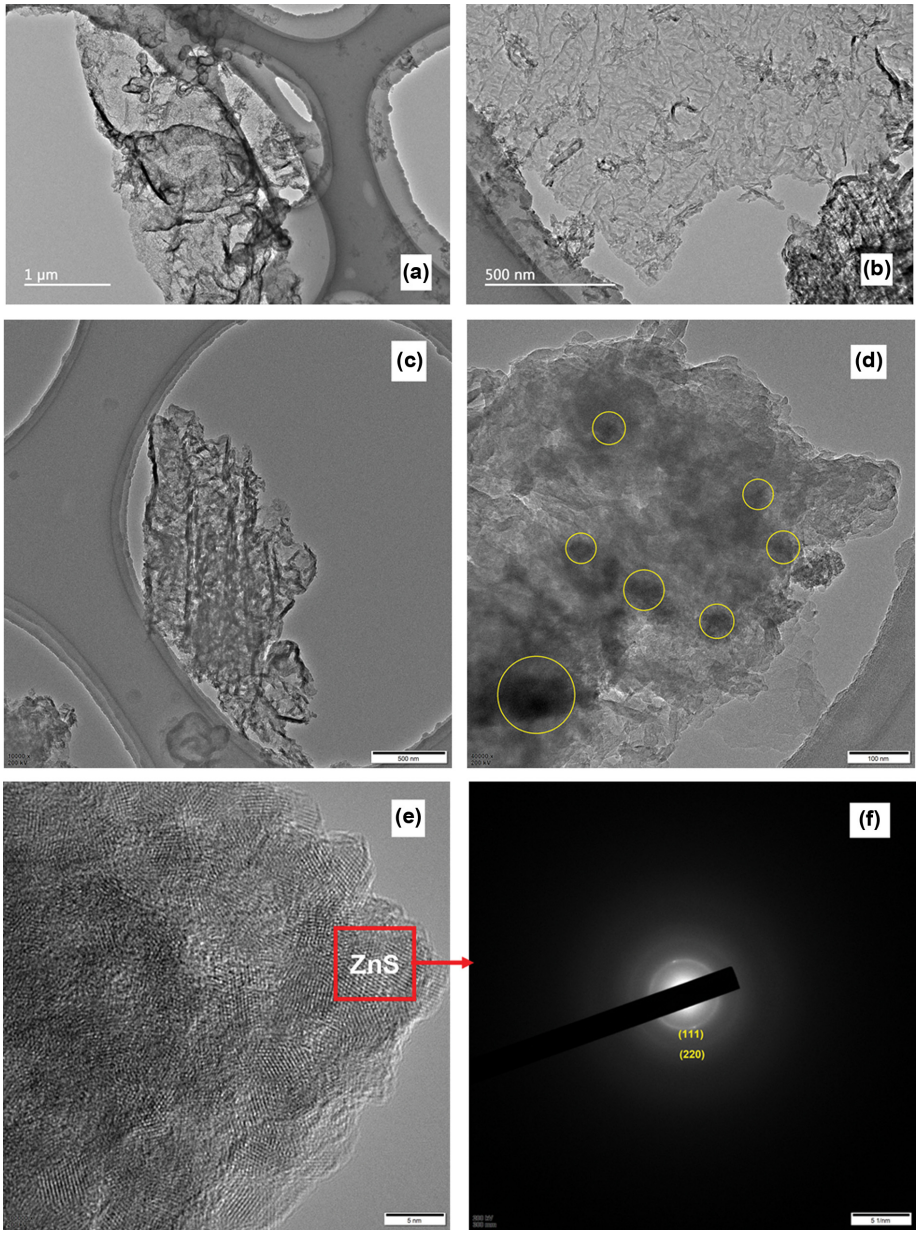

Fig. 4. TEM images of (a), (b) CNNS and (c), (d) 10ZnS/CNNS; (e), (f) SAED analysis of 10ZnS/CNNS.

[27].

The fine microstructures of CNNS and 10ZnS/CNNS were further investigated using TEM techniques. The TEM images in Fig. 4(a) and (b) testify the graphene-analogous morphology of as-synthesized CNNS, which displays an ultrathin two-dimensional nanosheet feature with thickness of dozens of nanometers and lateral size of few microns. Some darker portions are likely owing to the overlap of several nanosheets or a multilayer nanosheet. After impregnating with 10 wt% ZnS, the nanosheet structure of CNNS is still preserved (Fig. 4(c)). In addition, it can be found that the surface of CNNS is irregularly covered with many dark nanoclusters (dark spots in yellow circles) with uneven sizes (Fig. 4(d)), which are probably ascribed to ZnS grains. The high resolution transmission electron microscopy (HRTEM) photos with selected area electron diffraction (SAED) analysis are presented in Fig. 4(e) and (f). The diffraction rings of the (111) and (220) lattice planes of ZnS corresponding to interplanar spacings of 0.3238 and 0.1943 nm, respectively, are visibly detected, suggesting polycrystal structures of ZnS particles [28].

The chemical states and relative proportions of surface elements of the adsorbents were studied by using XPS technique. The XPS profiles of fresh and spent CNNS are presented Fig. 5. With respect to high-resolution C 1s spectra, the peaks at 284.9 and 285.6 eV are assigned to sp^2 hybridized C=C bonds [29]. The bands at 287.2-288.8 eV relate to the sp^2-bonded C atoms bonding to the N atoms inside the triazine rings (N=C-N) [30]. With respect to high-resolution N 1s profiles, the band at 397.4 eV likely belongs to cyanide groups (-C≡N) [31]. The bands at 398.2 and 398.8 eV correspond

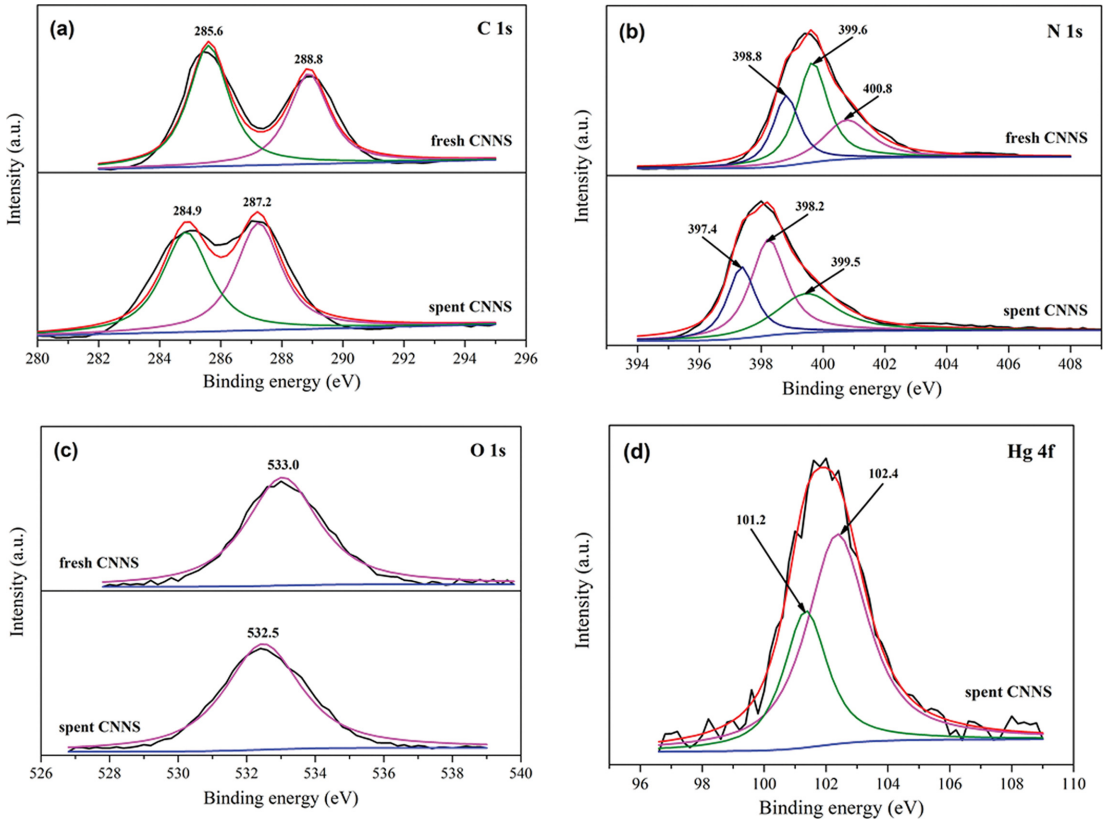

Fig. 5. XPS profiles of fresh and spent CNNS.

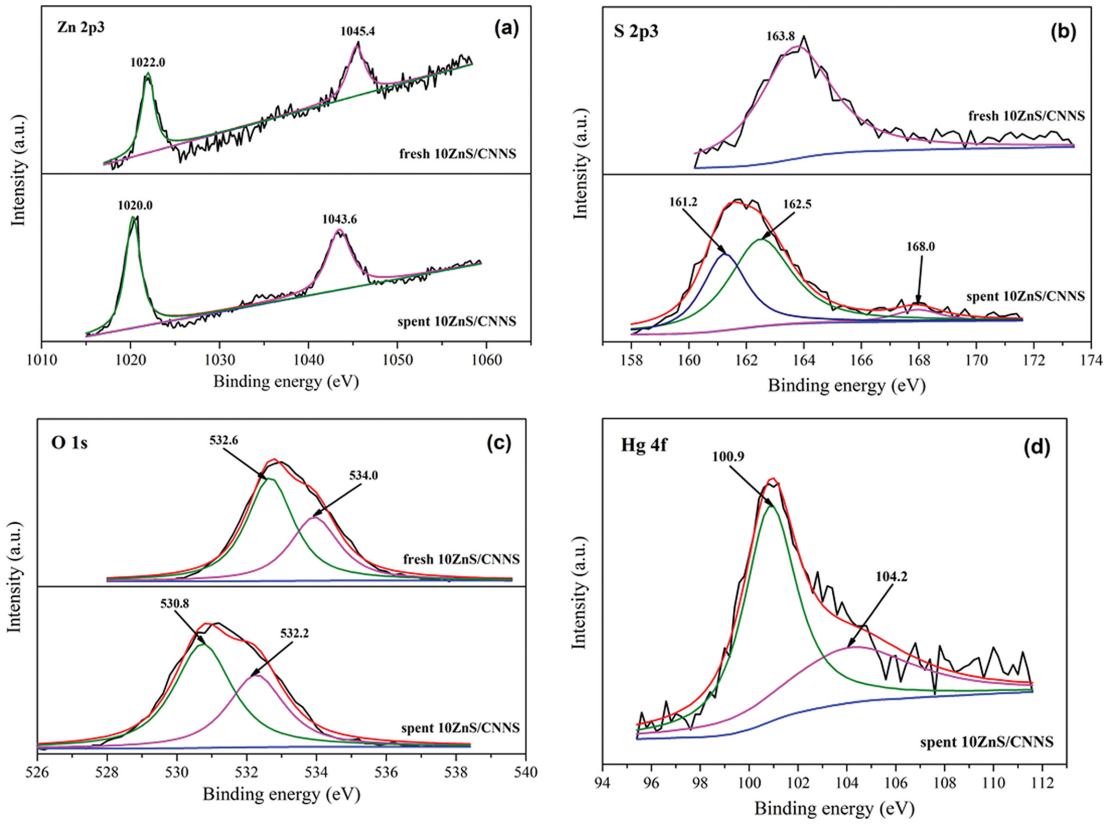

Fig. 6. XPS profiles of fresh and spent 10ZnS/CNNS.

to pyridinic-N (N-6) [32]. The peaks at 399.5 and 399.6 eV are plausibly ascribed to pyrrolic-N (N-5) [33]. The band at 400.8 eV is likely owing to amino functional groups (-NH_2) [34]. It can be found that the binding energies of C 1s and N 1s characteristic peaks visibly decline after mercury adsorption. This suggests that the adsorbed Hg^0 may donate electrons to the C and N atoms of CNNS. The bands at 532.5 and 533.0 eV are assigned to the oxygen in adsorbed carbonates or hydroxyls on adsorbent surface [35]. As for the Hg 4f spectrum of spent CNNS, the peak at 102.4 eV is attributed to Si 2p electron. The binding energy of mercury species at Hg $4f_{7/2}$ orbit of 101.2 eV is notably bigger than that of elemental mercury at Hg $4f_{7/2}$ orbit of 99.9 eV [36], suggesting the generation of oxidized mercury or coordinated mercury species.

The XPS spectra of fresh and spent 10ZnS/CNNS are displayed in Fig. 6. The doublet peaks at 1,020.0-1,022.0 eV and 1,043.4-1,045.4 eV are attributed to the Zn^{2+} species in ZnS [37]. The binding energy of Zn 2p3 noticeably moves toward lower values after mercury adsorption, indicating that Zn may accept electrons from the adsorbed Hg^0 to produce Zn-Hg amalgam as well. The peaks at 161.2 eV and 162.5-163.8 eV accord with sulfide (S^{2-}) and disulfide (S_2^{2-}) groups [38], respectively. The band at 168.0 eV in spent 10ZnS/CNNS is ascribed to the sulfate (SO_4^{2-}) groups [39], which probably stem from the oxidation of a portion of surface sulfur of ZnS by the oxygen from flue gas. After mercury adsorption, the featured peak of chemisorbed oxygen at 530.8 eV is distinctly detected [40]. This indicates that the gas-phase oxygen in flue gas can be chemisorbed on the surface of 10ZnS/CNNS, which may contribute considerably to the enhancement of its mercury removal performance. The Hg 4f spectrum of spent 10ZnS/CNNS displays two fitted peaks at 100.9 and 104.2 eV, which are visibly bigger than those of elemental mercury at Hg $4f_{7/2}$ orbit of 99.9 eV and Hg $4f_{5/2}$ orbit of 104.0 eV correspondingly [41], implying the generation of oxidized mercury species.

2. Mercury Removal Performance

The effect of ZnS loading value on the Hg^0 removal performance of CNNS at 100 °C is displayed in Fig. 7. Pristine ZnS and CNNS both exhibit relatively poor mercury capture ability with Hg^0 removal efficiency of 54.7 and 37.1%, respectively. Deposition

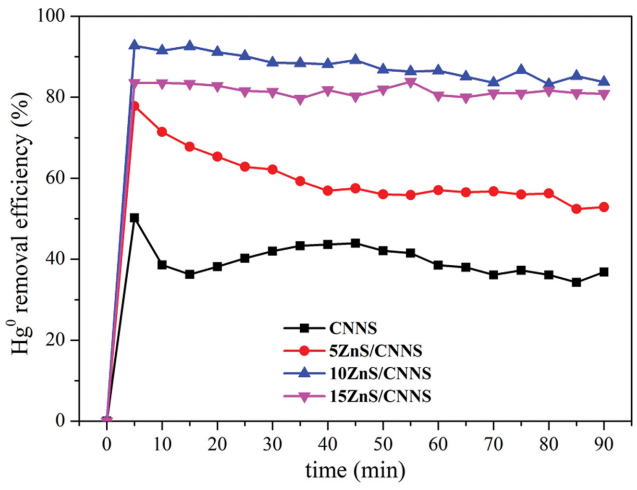

Fig. 7. Hg^0 removal performance of the as-prepared CNNS.

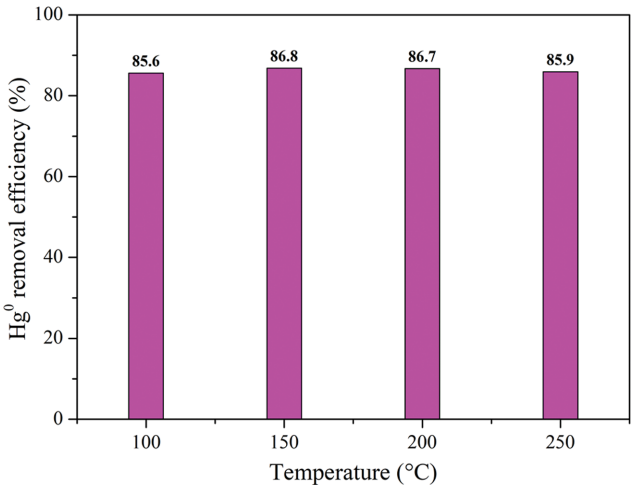

Fig. 8. Effect of adsorption temperature on Hg^0 removal efficiency of 10ZnS/CNNS.

of 5 and 15 wt% ZnS on CNNS can slightly improve its mercury removal efficiency to 43.0 and 51.3% correspondingly; however, they are still lower than that of pure ZnS. Minor loading of ZnS may not create sufficient active sites for Hg^0 oxidation, while an excess of ZnS deposition may cause aggregation of ZnS grains, both of which would lead to degradation of mercury removal performance to some extent. 10ZnS/CNNS notably outperforms pristine ZnS and CNNS with Hg^0 removal efficiency of 85.6%, which is plausibly owing to the synergy between ZnS and CNNS. Besides, 10ZnS/CNNS performs stably in the temperature range of 100-200 °C with mercury removing efficiency sustaining at 85.6-86.8% (Fig. 8). Thus, the optimal ZnS loading value should be 10 wt%.

3. Catalytic Oxidation Mechanism of Elemental Mercury

Conventional adsorbents capture flue gas elemental mercury via fixing Hg^0 on their surface active sites. Because the active sites on adsorbent surface are gradually occupied by mercury species, it is necessary to spray adsorbent continuously to achieve stable mercury removal performance. This would significantly increase capital cost and thus reduce the economics of power plants. Besides, considering that the waste heat in flue gas can be utilized, it is a meaningful mercury removal route to use thermal catalysis technology to convert elemental mercury into oxidized mercury, and coupled with existing WFGD system to control the total mercury emissions of power plants. Liu et al. [42] successfully studied the Hg^0 catalytic oxidation performance of diverse transition metal modified g-C_3N_4 via density functional theory. In this work, the structural model shown in Fig. 9 was adopted, where the clean CNNS (Fig. 9(a)) is a two-dimensional lamellar structure similar to graphene, in which C and N atoms are hybridized to form a highly delocalized π conjugated system. The Zn/CNNS structure is formed by doping zinc atom at the hole site of CNNS, and subsequent calculations are also carried out (Fig. 9(b)).

First, the adsorption performance of common reactants, namely gaseous elemental mercury and oxygen molecule, on the catalyst surface is considered. The specific adsorption structures are shown in Fig. S2 (Supplementary Materials). The corresponding adsorption energies are shown in Fig. 10. It can be seen that the adsorp-

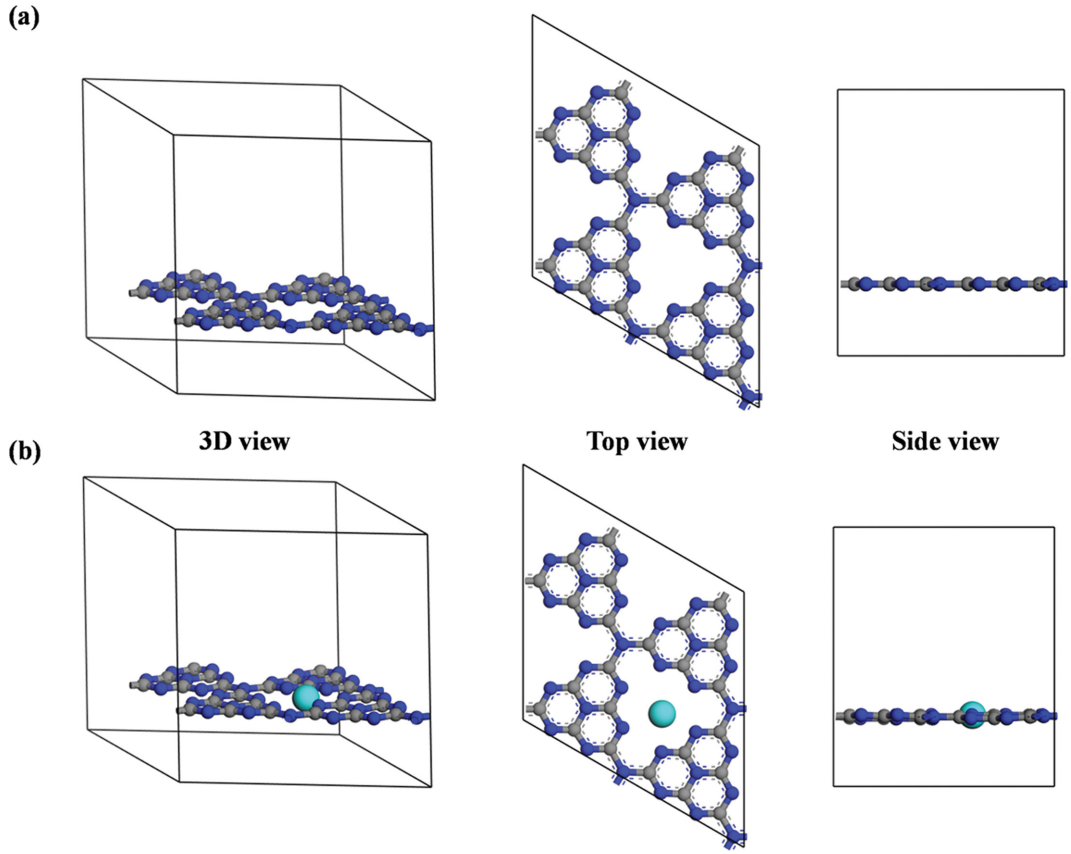

Fig. 9. DFT calculation models of the (a) CNNS and (b) Zn/CNNS (The gray ball denotes carbon, the blue ball denotes nitrogen, the cyan ball denotes zinc, and the same below).

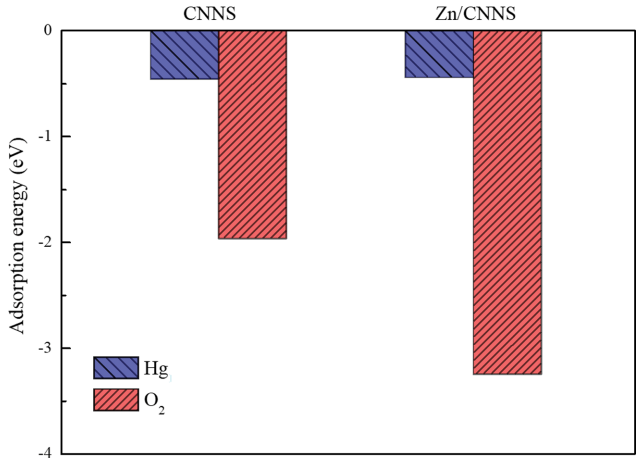

Fig. 10. Adsorption energy of gaseous Hg^0 and O_2 on the CNNS and Zn/CNNS surfaces.

tion energy of elemental mercury on clean CNNS and Zn/CNNS is very low, which is −0.457 and −0.441 eV, respectively. The adsorption energy of oxygen is very high, which is −1.963 eV on the surface of CNNS, indicating that oxygen is more easily adsorbed on the surface of catalyst compared with elemental mercury. In addition, the adsorption energy of oxygen on Zn/CNNS is also significantly enhanced, reaching −3.244 eV, indicating that the oxygen capture from flue gas can be effectively improved by doping Zn on CNNS surface. Considering the necessity of oxygen in the catalytic oxidation of elemental mercury, this improvement may play a key role in the mercury removal performances of modified samples.

The catalytic oxidation paths of gaseous elemental mercury on two surfaces are studied as shown in Fig. 11. In the reaction path of clean CNNS surface (the black line in Fig. 11), one oxygen molecule in flue gas is primarily adsorbed on the surface to form structure 1. An oxygen atom is bonded to the surface nitrogen atom, and the length of N-O bond is 2.286 Å. The O-O bond length is 1.265 Å, which is a slight increase compared to isolated oxygen (1.222 Å), which can be attributed to the interaction between surface O and N atoms. Then, the adsorbed oxygen splits on the surface and passes through the transition state TS1 to structure 2. This process (1-TS1-2) requires overcoming a reaction energy barrier of 4.146 eV and a positive reaction heat of 2.780 eV. In the transition state TS1, the distance between surface O and N atoms further shortens to 2.127 Å. The distance between the two oxygen atoms is also lengthened, reaching 1.583 Å. In structure 2, O atoms are separated and adsorbed on CNNS surface. One of the O atoms is bonded to surface N atom with a N-O bond length of 1.464 Å. Meanwhile, another O atom interacts with adjacent N and C atoms to form N-O bond of 1.479 Å and C-O bond of 1.629 Å, respectively. Subsequently, one gaseous Hg atom is adsorbed on the surface of O-containing CNNS (structure 3). The Hg atom is relatively

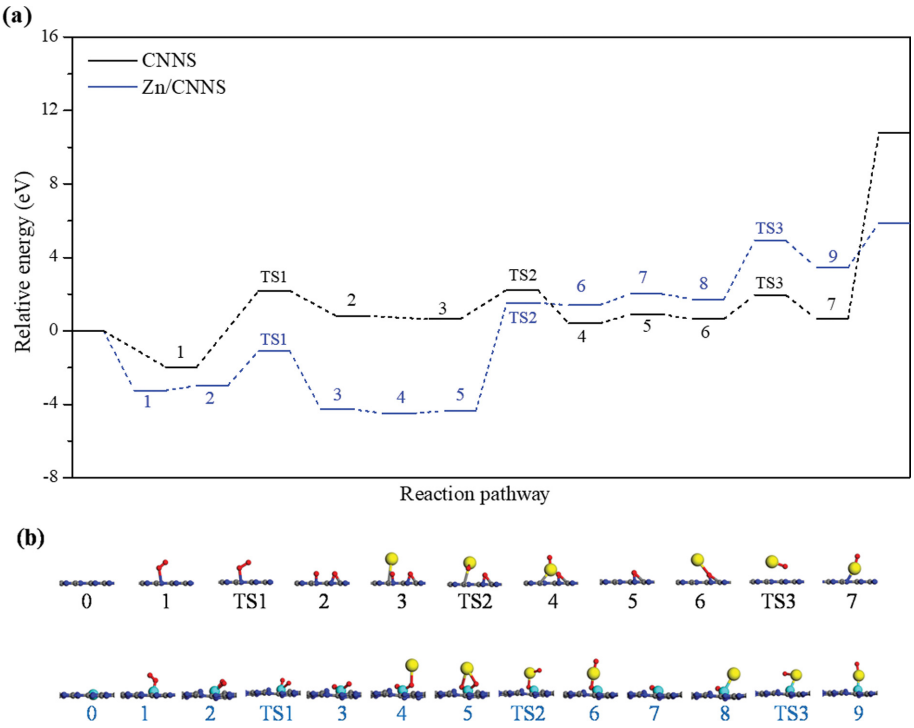

Fig. 11. Reaction pathway for the catalytic oxidation of Hg^0: (a) Energy profile of elementary steps; (b) Elementary reaction structures (The yellow ball denotes mercury and the red ball denotes oxygen).

far from CNNS surface with distance of 3.884 Å from the nearest C atom, which is also consistent with the adsorption energy analysis described above. This is followed by the first oxidation reaction of mercury (process 3-TS2-4), in which the adsorbed mercury reacts with adjacent surface oxygen to form mercury oxide. The HgO is attached to CNNS vertically by mercury atom in contact with the surface (structure 4). In transition state TS2, the distance between Hg atom and adjacent O atom gradually shortens to 2.625 Å. The Hg-O bond in the reaction product (structure 4) is 1.881 Å. The reaction step (3-TS2-4) has to overcome a reaction energy barrier of 1.606 eV and the total heat of reaction is −0.220 eV. Immediately, the first HgO product is desorbed from CNNS surface, which requires 0.490 eV of heat. At this point, an oxygen atom remains on the surface (structure 5), waiting for second mercury to attach and form structure 6. Finally, another mercury oxide is formed (6-TS3-7). As usual, Hg and O atoms are repositioned to form an HgO molecule. In transition state TS3, the distance of Hg-O bond is 2.191 Å. While in the product (structure 7), the Hg-O bond shortens to 1.922 Å. Mercury oxide desorption is then performed on the surface. This process requires overcoming a large energy of 10.131 eV, which is the rate-controlling step of the whole reaction.

However, the catalytic oxidation of elemental mercury on Zn/CNNS surfaces is different (see the blue line in Fig. 11). First, oxygen is adsorbed on the active site of zinc (structure 1), and the heat release in this process is –3.244 eV, which is significantly lower than oxygen adsorption on CNNS (−1.963 eV). The length of Zn-O bond is 1.910 Å, which is also shorter than that of oxygen adsorption in CNNS (N-O bond of 2.286 Å). The length of O-O bond in adsorbed oxygen is 1.335 Å, which is significantly longer than that of isolated oxygen (1.222 Å), indicating that Zn/CNNS surface is conducive to activating oxygen molecules and promoting the generation of surface reactive oxygen species. The oxygen then changes from monatomic adsorption to a diatomic co-adsorption state (structure 2) with O-O bond further stretching to 1.544 Å, which is slightly endothermic of 0.263 eV. Then, the co-adsorbed oxygen splits at the zinc active point, overcoming the reaction energy barrier of 1.871 eV. The net heat release of this reaction is −1.292 eV (2-TS1-3). In transition state TS1, the O-O distance is 2.550 Å, while in the reaction product (structure 3), the O-O distance goes up to 3.765 Å. It can be seen that the reaction energy barrier required for oxygen pyrolysis and activation on Zn/CNNS surface is significantly lower than that on CNNS surface (4.416→1.871 eV). In addition, the breaking of the O-O bond on Zn/CNNS surface is a thermodynamic spontaneous process of net exothermic heat (−1.292 eV), while on CNNS surface it is indeed an endothermic process (2.780 eV), which requires external heat injection.

From the above analysis, oxygen is more easily adsorbed than mercury on any of CNNS and Zn/CNNS surfaces; the significant activation of oxygen on the zinc-rich active point may be one of the important reasons for its superior mercury removal performance compared with clean CNNS. Next, mercury adsorbed on one of O atoms (structure 4) has lower adsorption energy of –0.213 eV and Hg-O distance of 3.028 Å. The Hg atom is then slightly displaced to transition between the two oxygen atoms, forming a co-adsorption state (structure 5). This process requires a slight heat of 0.126 eV. The distances between Hg and O atoms are 3.108 and 3.357 Å, respectively. Similarly, mercury reacts with an oxy-

gen atom, so that the oxygen atom is attached to the mercury atom and away from the catalyst surface (5-TS2-6). This process requires overcoming the reaction energy barrier of 5.887 eV and the total reaction heat absorption of 5.763 eV, which is the reaction rate control step of the overall reaction path. In transition state TS2, the bond between an oxygen atom and the active zinc point is broken, and moves closer to mercury. The Hg-O bond shortens (3.108→2.234 Å). The distance between Hg atom and other surface oxygen also shortens (3.357→2.573 Å). Immediately, the resulting mercury oxide is desorbed from the surface and forms structure 7, requiring an endothermic adsorption of 0.610 eV. The second Hg atom can be adsorbed on the active zinc site, exothermic adsorption of −0.292 eV. This adsorbed mercury reacts with surface reactive oxygen species to generate mercury oxide (8-TS3-9), which needs to overcome the reaction energy barrier of 3.199 eV and the total heat release of the reaction is 1.721 eV. Finally, the resulting mercury oxide is desorbed and the reaction is endothermic (2.425 eV). The catalyst surface is restored and the next cycle begins. Before and after the thermal catalytic process, the catalyst itself does not change, only needs to consume the oxygen from the flue gas, which can continuously transform the elemental mercury into oxidized mercury.

CONCLUSIONS

ZnS/g-C_3N_4 composites are employed for elemental mercury removal. Adding proper amounts of ZnS can reinforce the Hg^0 removal ability of CNNS. The optimal mercury removal performance was achieved over 10ZnS/CNNS within 100-200 °C, which is probably attributed to the synergy of ZnS and g-C_3N_4. The chemisorbed surface oxygen and polysulfide species probably accounted for the enhanced Hg^0 removal performance of 10ZnS/CNNS. DFT calculation shows that CNNS surface doped with zinc species can effectively improve its ability to capture oxygen from flue gas. The modified surface can split oxygen molecules and promote the generation of reactive oxygen species, thus improving Hg^0 catalytic oxidation performance.

ACKNOWLEDGEMENTS

This research is sponsored by National Natural Science Foundation of China (grant no. 52076126), Natural Science Foundation of Shanghai (grant no. 18ZR1416200), and Senior Talent Foundation of Jiangsu University (grant no. 18JDG017).

SUPPORTING INFORMATION

Additional information as noted in the text. This information is available via the Internet at http://www.springer.com/chemistry/journal/11814.

REFERENCES

1. C. T. Driscoll, R. P. Mason, H. M. Chan, D. J. Jacob and N. Pirrone, *Environ. Sci. Technol.*, **47**, 4967 (2013).
2. J. H. Pavlish, E. A. Sondreal, M. D. Mann, E. S. Olson, K. C. Galbreath, D. L. Laudal and S. A. Benson, *Fuel Process. Technol.*, **82**, 89 (2003).
3. E. G. Pacyna, J. Pacyna, K. Sundseth, J. Munthe, K. Kindbom, S. Wilson, F. Steenhuisen and P. Maxson, *Atmos. Environ.*, **44**, 2487 (2010).
4. K. C. Galbreath and C. J. Zygarlicke, *Fuel Process. Technol.*, **65-66**, 289 (2000).
5. S. X. Wang, L. Zhang, G. H. Li, Y. Wu, J. M. Hao, N. Pirrone, F. Sprovieri and M. P. Ancora, *Atmos. Chem. Phys.*, **10**, 1183 (2010).
6. H. Q. Yang, Z. H. Xu, M. Fan, A. E. Bland and R. R. Judkins, *J. Hazard. Mater.*, **146**, 1 (2007).
7. J. P. Yang, H. Xu, H. Chen, F. Meng, H. Zu, P. Zhu, Z. Q. Yang, M. Li and H. L. Li, *J. Hazard. Mater.*, **424**, 127336 (2022).
8. A. A. Presto and E. J. Granite, *Environ. Sci. Technol.*, **40**, 5601 (2006).
9. L. Zhao, C. T. Li, X. Zhang, G. Zeng, J. Zhang and Y. Xie, *Catal. Sci. Technol.*, **5**, 3459 (2015).
10. C. Lu, J. Wu and D. J. Liu, *Mater. Lett.*, **227**, 308 (2018).
11. H. Kaur, S. Singh and B. Pal, *Korean J. Chem. Eng.*, **38**, 1248 (2021).
12. J. Zhang, M. Zhang, L. Lin and X. C. Wang, *Angew. Chem. Int. Ed.*, **54**, 6297 (2015).
13. Z. Zhao, Y. Sun and F. Dong, *Nanoscale*, **7**, 15 (2015).
14. Y. T. Ngo, J. S. Chung and S. H. Hur, *Korean J. Chem. Eng.*, **37**, 1589 (2020).
15. D. J. Liu, Z. Zhang, L. Liu and J. Wu, *Surf. Rev. Lett.*, **27**, 2050017 (2020).
16. Z. Zhang, J. Wu and D. J. Liu, *Processes*, **7**, 279 (2019).
17. Z. Yang, H. L. Li, S. Feng, P. Li, C. Liao, X. Liu, J. Zhao, J. P. Yang, P. H. Lee and K. Shih, *Langmuir*, **34**, 8739 (2018).
18. H. L. Li, L. Zhu, J. Wang, L. Li and K. Shih, *Environ. Sci. Technol.*, **50**, 9551 (2016).
19. J. P. Yang, Q. Li, H. Zu, Z. Q. Yang, W. Q. Qu, M. Li and H. L. Li, *Environ. Sci. Technol.*, **54**, 16195 (2020).
20. J. D. Xiao, Q. Han, Y. Xie, J. Yang, Q. Su, Y. Chen and H. Cao, *Environ. Sci. Technol.*, **51**, 13380 (2017).
21. P. Niu, L. Zhang, G. Liu and H. Cheng, *Adv. Funct. Mater.*, **22**, 4763 (2012).
22. W. Liu, H. M. Xu, Y. Liao, Z. Quan, S. Li, S. Zhao, Z. Qu and N. Q. Yan, *Fuel*, **235**, 847 (2019).
23. D. J. Liu, C. Lu and J. Wu, *J. Nanopart. Res.*, **20**, 227 (2018).
24. S. Liu, L. Chen, X. Mu, M. Xu, J. Yu, G. Yang, X. Luo, H. T. Zhao and T. Wu, *Fuel*, **254**, 115537 (2019).
25. Y. Wu, W. Xu, Y. Yang, J. Wang and T. Zhu, *Catal. Sci. Technol.*, **8**, 297 (2018).
26. H. Li, Y. Jing, X. Ma, T. Liu, L. Yang, B. Liu, S. Yin, Y. Wei and Y. Wang, *RSC Adv.*, **7**, 8688 (2017).
27. J. A. Bearden, *Rev. Mod. Phys.*, **39**, 86 (1967).
28. H. Mao, J. Han, Y. Fu, Y. Song, C. Yu and X. Dong, *Appl. Catal. B-Environ.*, **102**, 417 (2011).
29. J. Xu, L. Zhang, R. Shi and Y. Zhu, *J. Mater. Chem. A*, **1**, 14766 (2013).
30. J. Zhang, M. Zhang, G. Zhang and X. C. Wang, *ACS Catal.*, **2**, 940 (2012).
31. J. F. Moulder, W. F. Stickle, P. E. Sobol, K. D. Bomben and J. Chastain, *Handbook of X-ray photoelectron spectroscopy: A reference book of standard spectra for identification and interpretation of XPS data*, Perkin-Elmer Corporation, Eden Prairie, Minnesota (1992).

32. J. Li, B. Shen, Z. Hong, B. Lin, B. Gao and Y. Chen, *Chem. Commun.*, **48**, 12017 (2012).
33. C. Wang, D. Wu, H. Wang, Z. Gao, F. Xu and K. Jiang, *J. Power Sources*, **363**, 375 (2017).
34. G. Dong, L. Yang, F. Wang, L. Zang and C. Wang, *ACS Catal.*, **6**, 6511 (2016).
35. D. J. Liu, W. G. Zhou and J. Wu, *Korean J. Chem. Eng.*, **33**, 1837 (2016).
36. N. D. Hutson, B. C. Attwood and K. G. Scheckel, *Environ. Sci. Technol.*, **41**, 1747 (2007).
37. S. L. Harmer, *Miner. Eng.*, **21**, 1005 (2008).
38. R. S. C. Smart, W. M. Skinner and A. R. Gerson, *Surf. Interface Anal.*, **28**, 101 (1999).
39. W. Liu, H. M. Xu, Y. Liao, Y. Wang, N. Q. Yan and Z. Qu, *Environ. Sci. Pollut. Res.*, **27**, 20469 (2020).
40. D. Jampaiah, S. J. Ippolito, Y. M. Sabri, J. Tardio, P. R. Selvakannan, A. Nafady, B. M. Reddy and S. K. Bhargava, *Catal. Sci. Technol.*, **6**, 1792 (2016).
41. J. Wilcox, E. Sasmaz, A. Kirchofer and S. S. Lee, *J. Air Waste Manage. Assoc.*, **61**, 418 (2011).
42. S. Liu, M. Xu, Y. Chen, J. Yu, C. Pang and T. Wu, *Fuel*, **305**, 121456 (2021).

Supporting Information

ZnS-modified carbon nitride nanosheet with enhanced performance of elemental Hg removal: An experimental and density functional theory study

Yang Ling*, Jiang Wu*,*,†, Lingtao Yang***, and Dongjing Liu**,†**

*School of Energy and Power Engineering, University of Shanghai for Science and Technology, Shanghai 200093, China
**School of Energy and Power Engineering, Jiangsu University, Zhenjiang 212013, China
***College of Energy and Mechanical Engineering, Shanghai University of Electric Power, Shanghai 200090, China
(*Received 15 September 2021 • Revised 15 December 2021 • Accepted 22 December 2021*)

Gaseous Elemental Mercury Removal

The as-prepared samples were tested for elemental mercury (Hg^0) removal at different temperature. For each test, 50 mg sample and a certain amount of glass beads (2 mm of diameter) were loaded into a vertical fixed-bed quartz reactor (6 mm of inner diameter, 700 mm of length) and then heated up to the given temperature (heating rate 5 °C/min). The N_2/O_2 mixed gas (95% N_2 and 5% O_2 by volume, 1.2 L/min) containing Hg^0 (produced by PSA mercury generator) flowed through the quartz glass tube continuously. The inlet and outlet Hg^0 concentrations were measured by an on-line mercury analyzer (Lumex, RA-915-M, Russia). The elemental mercury removal efficiency is calculated by the following formula:

$$\eta = \frac{[Hg^0]_0 - [Hg^0]}{[Hg^0]_0} \times 100\% \quad (1)$$

where $[Hg^0]_0$ represents the Hg^0 concentration (μg/m^3) at the reactor inlet, while $[Hg^0]$ represents the Hg^0 concentration (μg/m^3) at the reactor outlet.

Mulliken population analysis is shown in Table S1. It can be seen that the adsorption of mercury on pure CNNS is very weak. The mercury atom loses only 0.07 e of charges and becomes slightly positive. While, the interaction between Zn/CNNS and mercury is slightly enhanced, and mercury loses 0.22 e of charges and becomes partially positive. Similarly, pure CNNS interact weakly with oxygen, with two oxygen atoms change only 0.01 and −0.03 e, respectively. The interaction between Zn/CNNS and adsorbed oxygen is significantly enhanced. The two oxygen atoms lose a large amount of charges, yielding −0.37 and −0.27 e, respectively. The charge distributions before and after mercury adsorption are consistent with adsorption energies. The interaction between the surface and oxygen is even more intense.

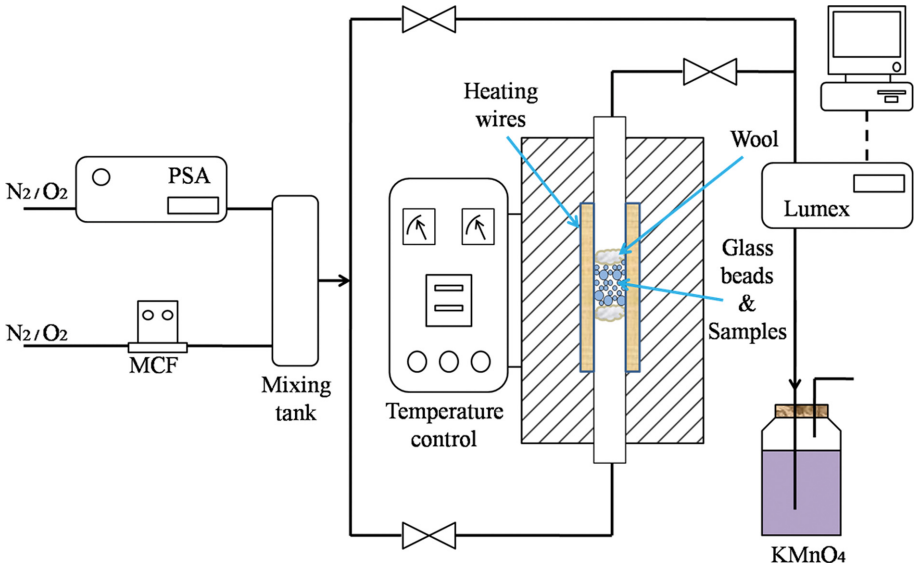

Fig. S1. Schematic of the gaseous elemental mercury removal system.

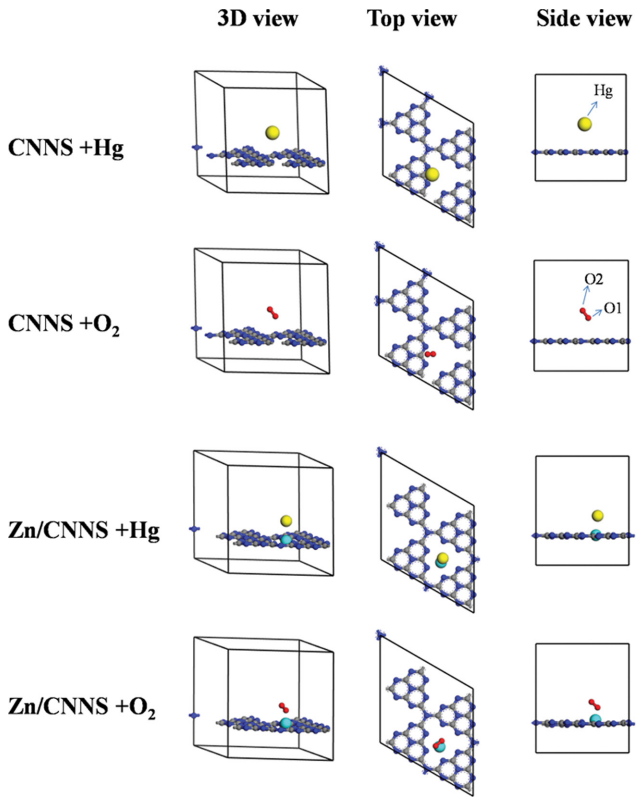

Fig. S2. Adsorption structure diagram of common reactants on CNNS surface (The gray ball denotes carbon, the blue ball denotes nitrogen, the cyan ball denotes zinc, the yellow ball denotes mercury and the red ball denotes oxygen).

Table S1. Mulliken atomic charge of atoms on adsorbate

Structure	Atom	Mulliken charge (e)
CNNS+Hg	Hg	0.07
CNNS+O_2	O1	0.01
	O2	−0.03
Zn/CNNS+Hg	Hg	0.22
Zn/CNNS+O_2	O1	−0.37
	O2	−0.27